

Lumen segmentation in magnetic resonance images of the carotid artery

Danilo Samuel Jodas^{a,c}, Aledir Silveira Pereira^b, João Manuel R. S. Tavares^{c,*}

CAPES Foundation, Ministry of Education of Brazil^a, Universidade Estadual Paulista “Júlio de Mesquita Filho”^b, Instituto de Ciência e Inovação em Engenharia Mecânica e Engenharia Industrial, Faculdade de Engenharia, Universidade do Porto^c

^a*Brasília - DF, 70040-020, Brazil*

^b*Rua Cristóvão Colombo, 2265, 15054-000, S. J. do Rio Preto, Brazil*

^c*Rua Dr. Roberto Frias, s/n, 4200-465, Porto, Portugal*

Abstract

Investigation of the carotid artery plays an important role in the diagnosis of cerebrovascular events. Segmentation of the lumen and vessel wall in Magnetic Resonance (MR) images is the first step towards evaluating any possible cardiovascular diseases like atherosclerosis. However, the automatic segmentation of the lumen is still a challenge due to the low quality of the images and the presence of other elements such as stenosis and malformations that compromise the accuracy of the results. In this article, a method to identify the location of the lumen without user interaction is presented. The proposed method uses the modified mean roundness to calculate the circularity index of the regions identified by the K-means algorithm and return the one with the maximum value, i.e. the potential lumen region. Then, an active contour is employed to refine the boundary of this region. The method achieved an average Dice coefficient of 0.78 ± 0.14 and 0.61 ± 0.21 in 181 3D-T1-weighted and 181 proton density-weighted MR images, respectively. The results show that this method is promising for the correct identification and location of the lumen even in images

*Corresponding author. Tel.: +351 22 508 1487; fax: +351 22 508 1445

Email addresses: daniلودas@gmail.com (Danilo Samuel Jodas), aledir@sjrp.unesp.br (Aledir Silveira Pereira), tavares@fe.up.pt (João Manuel R. S. Tavares)

URL: <http://www.fe.up.pt/~tavares> (João Manuel R. S. Tavares)

corrupted by noise.

Keywords: Magnetic Resonance Imaging, K-means algorithm, Deformable model, Subtractive clustering, Circularity index

1. Introduction

The segmentation of medical images is an important diagnostic tool to detect and/or to follow-up various diseases. An examination of the arterial system allows the identification of pathologies associated to cardiovascular diseases [1, 2]. One of the main cardiovascular diseases is atherosclerosis, which is when fatty components, calcium, cholesterol and fibrous tissues form plaques on the artery walls. Consequently, atherosclerosis reduces or blocks the blood flow through the artery, which can cause amaurosis fugax and strokes [3, 4, 5]. Several imaging modalities are able to identify atherosclerosis in a non-invasive way, allowing treatment planning before the onset or recurrence of symptoms.

Magnetic Resonance Imaging (MRI) of the carotid artery has been widely used in studies to identify the atherosclerotic plaques and their main components in order to analyze the progression of the disease [6]. However, the correct identification of the lumen and vessel boundaries is an important step before segmenting the atherosclerotic plaque components, since atherosclerosis is located between those boundaries. The automatic/semi-automatic segmentation of the lumen and vessel wall has been proposed in several studies and in most cases it is considered as the first step to identify and evaluate atherosclerosis [7, 8, 9, 10, 11, 12]. However, this task is not always performed automatically and therefore, in several studies, the boundaries of the lumen and vessel wall in the images have to be delineated manually [9, 13]. Typically, the lumen boundary is located inside the vessel wall. Hence, the lumen boundary can be extended until it reaches the vessel wall boundary [8].

Three-dimensional ultrasound (3D-US) is also an interesting imaging modality to envisage the anatomy of the carotid artery [14, 15, 16]. However, the segmentation of lumen and wall boundaries in 3D-US images is a challenge be-

cause of the poor contrast and weak boundaries caused by shadows that are due to calcifications; however, several studies have been proposed to overcome such difficulties [17, 18].

30 The segmentation of the lumen and wall of the carotid artery is a strong focus of research due to the lack of automation. Although the refinement of the lumen boundary can be easily achieved by deformable models [19, 20, 21], finding the region corresponding to the lumen is the most important step towards a fully automatic segmentation.

35 The semiautomatic segmentation of the lumen and wall of the carotid artery was tackled by Adame et al. [22, 23]. In those studies, ellipse fitting was used to detect the vessel wall boundary, while fuzzy clustering was applied to identify the lumen and carotid plaques. Although the segmentation results had high correlation with the manual segmentations, the method requires user interaction
40 to determine the centre point of the lumen.

Another study carried out by Saba et al. [8] proposed the segmentation of the lumen and wall of the carotid artery based on the level set algorithm. The radial expansion from a specific point is used to define the initial contour of the lumen. The final contour of the lumen, which is expanded by two pixels, is then
45 used to initialize the contour of the carotid wall.

An attempt to automatically segment the lumen in transverse ultrasound images of the carotid artery was undertaken by Yang et al. [24]. The proposed method used the Canny algorithm to find the edges in the input image and the morphological closing operation was used to find and fill the region correspond-
50 ing to the lumen.

Gao et al. [25] proposed a method to identify the media-adventitia and lumen regions on intravascular ultrasound (IVUS) images by applying an adaptive region growing algorithm and the combination of the K-means and 2D Otsu algorithms to identify the lumen inside the media-adventitia region. The al-
55 gorithms were applied individually and the minimization of the curvature was used to obtain the region with the least curvature variation, which is the best representation of the lumen.

Santos et al. [26, 27] addressed the segmentation of the lumen and bifurcation of the common carotid artery in B-mode ultrasound images. After a binarization process, the binary image containing the region corresponding to the lumen was used to generate the masks that were applied in the segmentation of the lumen and bifurcation boundaries. The Chan-Vese segmentation algorithm correctly detected the inferior and superior lumen walls. Although the segmentation was fully automatic, the method is only for longitudinal B-mode ultrasound images.

This study proposes a fully automatic method to identify the location of the lumen in MR images of the carotid artery. This method relies on the analysis of the regions in the input image to identify the ones corresponding to the potential lumen. We hypothesized that, since the lumen is a low intensity region with an approximately circular shape on axial MR images, the use of the mean roundness index would allow the identification of the region with the maximum circularity that may represent the potential lumen. In addition, an active contour method is applied to refine the region boundaries. In order to evaluate the method, a comparison between the computer and manual segmentations was made to attain a quantitative analysis.

The article is organized as follows: the steps of the proposed method are described in Section 2. The results of the segmentation, as well as the comparison with the manual segmentation, are presented in Section 3. Section 4 points out the advantages and limitations of the proposed method. Finally, the conclusions are drawn in Section 5.

2. Materials and Methods

2.1. Image acquisition

The MR images of the carotid artery selected for this study were used in research by van Engelen et al. [9] and kindly provided by the authors on request. The proposed method was performed on images that are the regions of interest surrounding the carotid arteries. A registration procedure was previously

performed to match the original MR images with the corresponding histology images, which only contained the region of the artery under study [9]. Once the matching was completed, the MR images were cropped to obtain only the part that matched the histology images [9]. The original dataset was composed of five MRI scans acquired from thirteen patients: T1-weighted (T1W), Proton Density Weighted (PDW), Time-of-Flight (TOF) and two 3D-T1W scans. The first three MRI scans were acquired without administration of intravenous (IV) contrast media, whereas the 3D-T1W scan was acquired with and without contrast media. The post-contrast 3D-T1W scan was performed 4.6 ± 3.4 minutes after the administration of the contrast media. Each MRI scan is composed of approximately 17.7 ± 4.8 slices per patient; each slice has a pixel size of $0.25 \text{ mm} \times 0.25 \text{ mm}$. Computer Tomography Angiography (CTA) images were also acquired to provide details for the registration with the histology images and to facilitate the manual segmentation of the lumen, vessel wall and plaque components. Manually drawn contours of the lumen and arterial wall were also provided for many of the MR slices. The manual delineations of the lumen and vessel wall were performed by one expert based on the combination of the CTA, PDW and post-contrast 3D-T1W scans with visual assessment of additional *in vivo* MRI scans [9]. More details about the MRI scans are available in van Engelen et al. [9].

From the original image dataset, we used all MR images with their corresponding ground truth, i.e. one reference contour of the lumen and another one for the vessel wall manually delineated in the slice under analysis; hence, 181 3D-T1W and 181 PDW MR images were used in the experiments.

2.2. Methodology

The proposed method is made up of three main stages, as shown in Figure 1.

The pre-processing stage is necessary to minimize noise and improve the quality of the input images. Then, the enhanced images are submitted to the segmentation stage in order to separate the regions with low pixel values, which

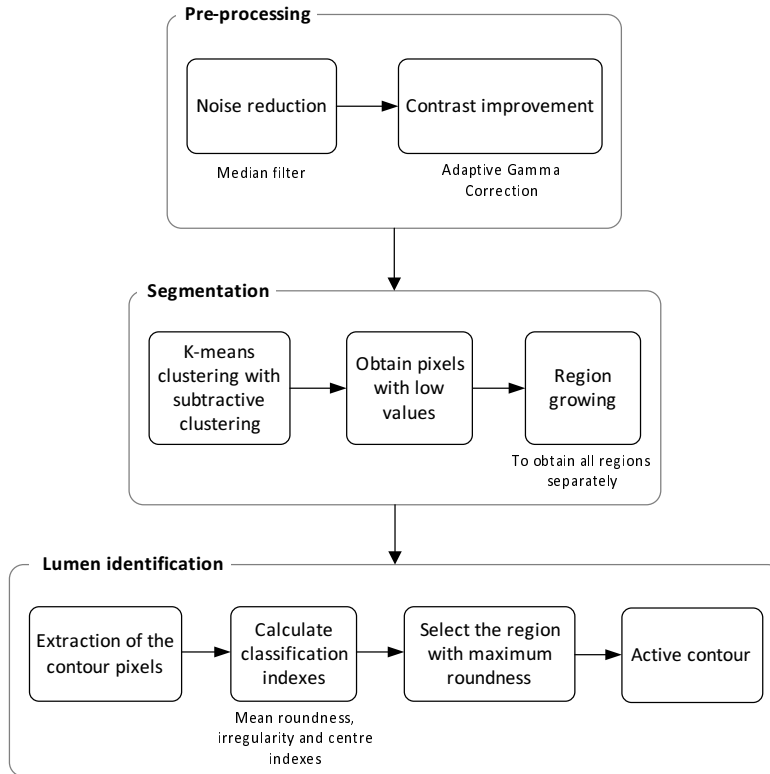


Figure 1: : Diagram of the proposed segmentation method.

include the background and the lumen regions. The lumen identification stage uses three classification indexes to identify the region corresponding to the lumen of the artery, which is then inputted to an active contour algorithm for further refinement of the boundary.

2.2.1. Pre-processing

The first step of the pre-processing stage is the use of a median filter with a mask of 5×5 to minimize the noise effects in the original images. The median filter was chosen due to its ability to remove noise without compromising the boundaries of the regions of interest.

The contrast enhancement step improves the brightness of the dark regions of the input images. The transformed-based gamma correction algorithm used

here is a contrast enhancement algorithm belonging to the group of histogram modification-based algorithms [28]. In order to overcome the under- and over-
130 estimation problems of the common gamma correction and histogram equalization algorithms, Huang et al. [28] proposed a gamma correction-based method to avoid the overestimation of regions with low-level intensities. The method relies on the probability density function (PDF) and the cumulative density function (CDF) of the intensity values:

$$T(l) = l_{max} \times (l/l_{max})^{1-CDF(l)}, \quad (1)$$

135 where $CDF(l)$ is the cumulative density function of the intensity value l and l_{max} is the highest possible intensity value. The output intensity $T(l)$ progressively increases as the CDF increases. Also, a weighting distribution is used to avoid an overestimation of low-level intensities. The weighting PDF is proposed as:

$$pdf_w(l) = pdf_{max} \times \left(\frac{pdf(l) - pdf_{min}}{pdf_{max} - pdf_{min}} \right)^\alpha, \quad (2)$$

where l is the intensity value, pdf_{min} is the minimum probability of the PDF
140 function, pdf_{max} is the maximum probability and α is a parameter. The weighting CDF is defined as:

$$cdf_w(l) = \sum_{l=0}^{l_{max}} \frac{pdf_w(l)}{\sum pdf_w}, \quad (3)$$

where l_{max} is the highest possible intensity value and $\sum pdf_w = \sum_{l=0}^{l_{max}} pdf_w(l)$. The adaptive gamma correction with weighting distribution (AGCWD) [28] is:

$$T(l) = l_{max} \times (l/l_{max})^{1-cdf_w(l)}. \quad (4)$$

The amount of contrast enhancement depends on the value of the α parameter. The larger α is, the greater the enhancement will be.
145

Since the correct contrast enhancement plays an important role in the segmentation accuracy, the AGCWD is used in this study to avoid overestimating

the brightness of the input images. However, a potential loss of important information can occur due to this image processing. Therefore, the analysis of the grayscale intensity is important to automatically determine whether the contrast correction is necessary or not. Hence, an automatic determination technique of the contrast enhancement of images based on the PDF of the grayscale intensities is proposed here. The PDF of the grayscale intensities is partitioned into two halves: the first halve represents the low intensity pixels of the image, whereas the second one represents the high intensity pixels. The difference between the accumulated probabilities of both halves is calculated. If the difference is low, the input image has a good contrast. The Otsu threshold is used to separate the probability density function. The following equation represents the basis of the automatic contrast correction:

$$D = \sum_{i=1}^t PDF_{min_i} - \sum_{j=t+1}^N PDF_{max_j}, \quad (5)$$

where PDF_{min} and PDF_{max} represent the probabilities of the low and high intensities of the input image, respectively, t is the value obtained by the Otsu threshold algorithm and N is the highest possible intensity value. If D is equal or less than a threshold, the contrast correction is not necessary. Here, a threshold value of 0.1 was found to be the one that led to good contrast enhancements without compromising the structures under analysis.

2.2.2. Segmentation

The K-means clustering algorithm is a well-known method to separate regions with similar characteristics (of intensity, for instance) in images. However, the correct use of the cluster centroids used in the K-means algorithm is a challenging task because different images have different cluster centroids. Additionally, trial and error is not an adequate approach because it is time consuming. Therefore, an automatic method to determine the cluster centroids is necessary.

The inconsistency results of the Fuzzy C-means algorithms are caused by different membership values generated by several executions. Thus, different

175 cluster centroids can be generated because they are calculated from the membership values.

Subtractive clustering [29] has been proposed as an alternative approach to avoid the instability of the Fuzzy C-means algorithms. The adequate number of cluster centroids is calculated from the potential of each pixel in the neighbourhood as:

$$P_i = \sum_{j=1}^n e^{\frac{-4\|x_i - x_j\|^2}{r_a^2}}, \quad (6)$$

where $\|x_i - x_j\|$ represents the distance between pixels x_i and x_j , r_a is the radius representing the neighbourhood and n is the number of pixels in the input image. Equation 6 gives the initial potential of each pixel; then, the pixel having the highest potential is selected as the first cluster centroid. The next centroids are found according to:

$$P_i = P_i - P_j \times e^{\frac{-4\|x_i - x_j\|^2}{r_b^2}}, \quad (7)$$

where P_j represents the highest potential, x_j is the pixel with highest potential and r_b is the radius representing the neighbourhood. Equation 7 reduces the potential of the neighbouring pixels; then, the next pixel with the highest potential is selected as the next cluster centroid and the process is repeated until all the centroids have been found.

The advantage of the subtractive clustering algorithm is that the cluster centroids do not change in different runs. This is due to the fact that the potential function relies on the pixel values only (or another feature calculated from the pixels of the input image).

195 After the cluster centroids have been found, a clustering algorithm may be applied. The combination of the K-means algorithm with the subtractive clustering proposed by Dhanachandra et al. [30] was used in this study. Considering the fact that regions having similar grayscale intensities can be merged into one cluster, the choice of the number of clusters plays an important role to determine the correct segmentation of the lumen. The merging of the lumen region

with pixels of the background can occur in arteries with a thin and low intensity wall. The lower the number of clusters, the higher the probability that the lumen and the background regions become one cluster. Based on several experiments, four clusters were found to be a stable choice to correctly identify
205 the region corresponding to the lumen in the images tested.

Because the lumen and the background usually have low intensities in MR images, the next step selects the regions belonging to the cluster with low intensity. An image with such regions is returned as a binary image, in which the regions are represented as white and the background as black. The image is
210 then submitted to the region growing algorithm in order to obtain all regions of the image separately. Here, the region growing is performed on the image corresponding to the cluster with low intensity values to obtain a set with all regions of interest. The white pixels have been chosen as the seed of the region growing algorithm, and the regions are merged when the pixels in the neighbourhood do
215 not belong to another region previous identified and have the same intensity as the seed. When a region is found, another pixel not belonging to the identified region is chosen as the seed and the process continues until all regions have been found. Although the region growing algorithm has been chosen to separate the regions, the connected component labelling algorithm could also be used to per-
220 form the same task without loss of performance. Examples of the segmentation stage with and without previous contrast enhancement are depicted in Figures 2 and 3.

2.2.3. Lumen identification

The lumen identification stage is the kernel of this study, which uses measures
225 to evaluate each region of interest obtained in the previous stage. Since the lumen is a region similar to a circle, a set of indexes that maximize the function representing the roundness of the possible region corresponding to the lumen is calculated. Hence, three indexes are found for each region in the segmented image:

- 230 • Circularity index (MR);

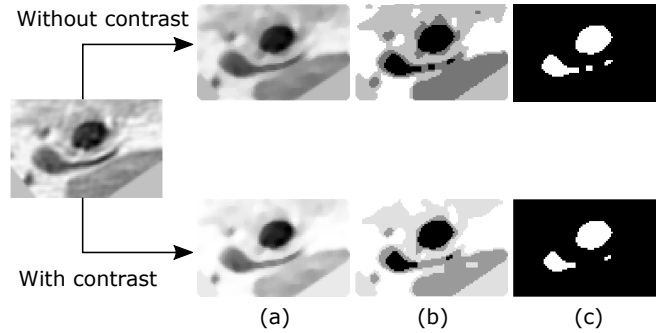


Figure 2: Example of the segmentation stage obtained from the 3D-T1W image with and without previous contrast enhancement; the image obtained from the median filter is shown in (a); the clustered image is shown in (b); and finally, the clusters of the low intensity pixels found are shown in (c).

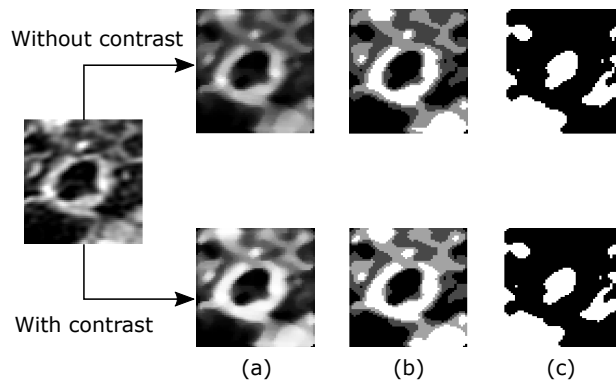


Figure 3: Example of the segmentation stage obtained from the PDW image with and without previous contrast enhancement; the image obtained from the median filter is shown in (a); the clustered image is shown in (b); and finally, the clusters of the low intensity pixels found are shown in (c).

- Irregularity index (Ir);
- Centre index (d).

The process to identify the lumen requires maximizing a function composed of the above-mentioned indexes. In order to avoid additional processing and increase the performance of the method, regions with less than 1.5% of the total number of pixels of the input image are discarded since they are usually

associated to noise. The indexes of all remaining regions are calculated.

Circularity indexes have been proposed in several studies [31, 32, 33] to quantify the roundness of regions in images. Ritter and Cooper [32] proposed a new index for determining the circularity of objects in images. The new index is called mean roundness, which represents the ratio between the average radius and the distance between the radius of each border pixel and the average radius:

$$MR = \frac{1}{N} \sum_{i=1}^N \frac{\bar{r}_b}{|r_i - \bar{r}_b| + \bar{r}_b}. \quad (8)$$

The larger the mean roundness (MR) index is, the more circular the object under analysis is. The proposed circularity index is independent of the image resolution [32].

An additional term was added to the mean roundness index to avoid pixels at the border of the input image:

$$MR = \frac{1}{N} \left(\sum_{i=1}^N \frac{\bar{r}_b}{|r_i - \bar{r}_b| + \bar{r}_b} \right) - n_b, \quad (9)$$

where n_b is the number of pixels of the region that are located at the border of the image. The modified MR index tries to reduce the circularity index of regions at the border of the input image. Also, since no rotation, translation or scaling transforms are performed in the proposed method, the location of the regions on the input image does not change.

In addition to the mean roundness index, the irregularity index has also been proposed to avoid regions with irregular contours. The following irregularity index was used in this study:

$$Ir = P * \left(\frac{1}{SD} - \frac{1}{GD} \right), \quad (10)$$

where P is the number of pixels of the contour, SD is the shortest diameter and the GD is the largest diameter [34]. If the difference between SD and GD is equal to 0 (zero) or close to it, the Ir index decreases, which means that the boundary is more regular.

260 In addition, a centre index (d) is used to identify the correct location of the lumen. In general, the lumen is located close to the centre of the image. Hence, the distances between the centre of the image and the centre of each region are calculated and used to maximize the final index function. Hence, the inverse of the irregularity and centre indexes are then used to maximize the proposed
265 circularity index for each region accordingly to:

$$E = MR + \frac{1}{Ir} + \frac{1}{d}. \quad (11)$$

The irregularity and centre indexes are used to penalize the mean roundness index of regions with irregular borders and those far from the centre of the input image, respectively. The lower the irregularity index is, the larger its inverse will be. The same concept is also applied to the inverse of the centre
270 index. Therefore, regions with high MR , irregularity and centre index values have a high probability of being the lumen.

The region that maximizes the circularity index is then submitted to the Chan-Vese active contour algorithm [20] in order to refine the contours previously found. The binary image representing the lumen region may not fit the
275 true boundary of the lumen in the MR image. Hence, the contour of such a region is used as the input of the Chan-Vese active contour model, which is applied to the original image in order to fit the contour to the true boundary. This refinement step plays an important role to avoid under- or over-estimation of the contour, leading the contour closer to the true boundary of the lumen
280 under analysis and, consequently, better results.

The Chan-Vese active contour was proposed by Chan and Vese [20] to segment the boundaries of objects in images based on the level set and Mumford-Shah models. The Chan-Vese active contour model is based on the energy minimization of the variations inside and outside the region as a level set prob-
285 lem, which can deal successfully with topological variations. Since the gradient of the image is not used in the Chan-Vese model, the method is recommended for the segmentation of medical images which commonly have weak boundaries

of the structures under analysis.

2.3. Quantitative analysis

290 The proposed method was validated by evaluating the contours and the areas of the regions found. The following measures were used to compare the segmentations of the new method and the manual method:

- Dice coefficient;
- Polyline distance;
- 295 • Hausdorff distance.

The Dice coefficient represents the overlap between two regions, which is a ratio between the intersection and the union of the regions. Here, this metric is important to assess the under- or over-segmentation of the region identified by the automatic method with respect to the corresponding manual method.

300 The polyline distance represents the average minimum distance between two sets of points, i.e. image pixels, whereas the Hausdorff distance provides the maximum between the greatest distances between such points.

Under- and over-estimation of the lumen affect the value of the Dice coefficient, since it represents the ratio between the intersection and union of the regions under analysis. However, the centroid difference between the manually segmented and the automatically segmented lumen is low when the algorithm finds the correct location of the lumen, even when the Dice coefficient is reduced. Therefore, the difference between the centroids of the regions corresponding to the manual segmentation and the automatically segmented lumen is calculated by using the Euclidean distance. The higher the Euclidean distance, the farthest the regions are from each other.

3. Results

The proposed method was performed on each slice of the post-contrast 3D-T1W and PDW images with the ground truths provided. The following parameters were used to perform the automated segmentation: the mask of the median

315

filter was set to 5×5 ; when it was necessary to adjust the contrast, the value of α in Equation 2 was defined as equal to the difference between the probabilities of the low and high intensities, as described by Equation 5; the radius r_a and r_b used in the subtractive clustering were set to 1.2 and 1.8, respectively; the percentage of disregarded regions was set at 1.5%; and the number of iterations of the Chan-Vese active contour algorithm was set to 200. The 5×5 mask was empirically determined as the most suitable template for removing noise from the images without disturbing the edges of the regions of interest. The radius values r_a and r_b of the subtractive clustering were empirically determined through several tests as the most appropriate parameters for separating the regions of the input images. In addition, the percentage of the disregarded regions was also experimentally found as the most suitable one for the resolution of the images under evaluation. A higher percentage value could remove a region corresponding to the lumen, particularly in images where the lumen is small. The values of all parameters were kept constant in the experiments. Examples of the segmentation results and corresponding manual segmentation are shown in Figure 4.

In Figure 4, the green contours represent the results of the proposed method, whereas the red contours represent the manual results. The lumen was correctly identified by the proposed method as shown by the two results. The values of the validation measures corresponding to the results shown in this figure (Figure 4) are given in Table 1.

Table 1: Values of the validation measures for the images in Figure 4.

	Dice	PD(px)	HD(px)	CD(px)
slice 1	0.75	2.05	5	2.03
slice 2	0.77	1.51	4.12	1.90
slice 3	0.80	1.26	5	3.59
slice 4	0.56	2.56	5	3.75
slice 5	0.78	1.58	4.24	2.82
slice 6	0.51	3.62	9.22	2.72

*PD = Polyline distance; HD = Hausdorff distance
CD = Centroid distance; px = pixels

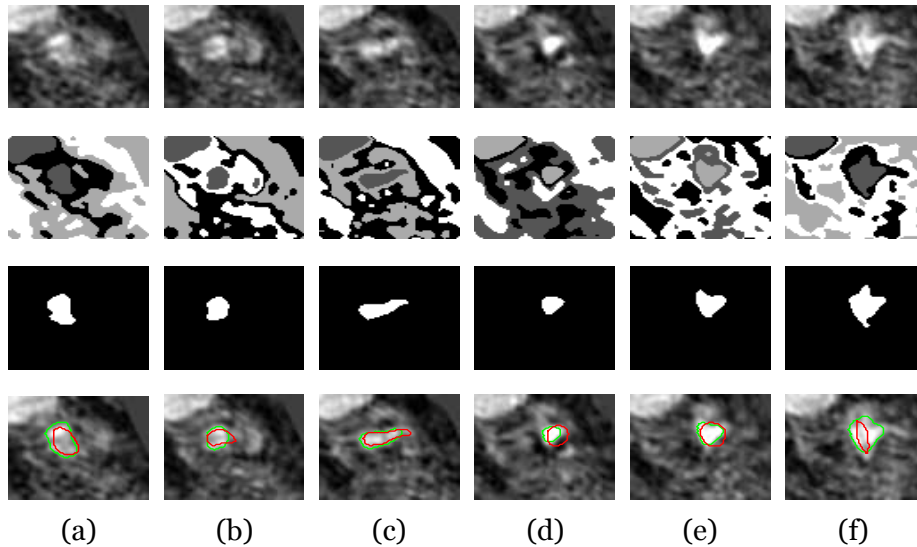


Figure 4: Examples of segmentation results obtained from the 3D-T1W images: Each column represents one image belonging to patient 1, which is composed of six slices with ground truth; the first row contains the input images; the second row represents the results of the K-means with subtractive clustering; the third row shows the images with the lumen that was identified by taking into account the modified mean roundness index; and finally, the fourth row shows the refined contour in green and the manual one in red.

The automatic segmentation obtained for slice 6 of patient 1 in Figure 4f, shows that the result was overestimated compared to the manual one; however, it should be understood that the centroids of both regions were well matched.

In order to show the impact of the centre index and the regions on the border of the input image on the segmentation results, the images obtained with and without taking this index and these regions into account are shown in Figure 5.

The identified region in Figure 5a does not correspond to the correct location of the lumen, despite its high value of mean roundness index. The correct lumen is represented by the brightest circular area close to the centre of the image. In this case, the centre index penalizes the value of the mean roundness index of the region close to the right top of the image, reducing the value of this index. The result obtained with the centre index activated is shown in Figure 5b. For the cases with regions that include pixels on the border of the input image, the

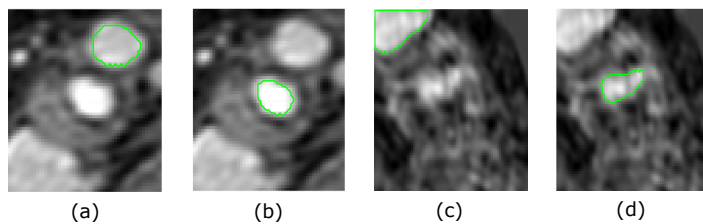


Figure 5: Impact of the centre index (a - not taken into account and b - taken into account) and of the regions on the border of the input image (c - not taken into account and d - taken into account) on the segmentation of the lumen region.

impact of the number of these pixels on the mean roundness index is illustrated in Figures 5c and 5d. Here the number of these pixels contributes to reduce the mean roundness index of such regions, which leads to good segmentation results (Figure 5d).

355 Figure 6 illustrates the influence of the refinement process of the segmentation contour on the final result. In this figure, the red contour represents the contour of the binary mask of the lumen identification step, whereas the green contour is the result of the Chan-Vese active contour, i.e. the result of the refinement process from the red contour. In all cases shown in this figure, the
 360 initial contour (in red) underestimated the true boundary of the lumen, which was then corrected by the Chan-Vese model (green contour).

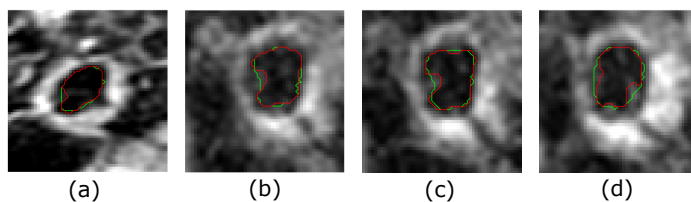


Figure 6: Impact of the Chan-Vese active contour on the final segmentation result: The red contour is the one obtained in the lumen identification step, and the green contour is the one obtained by the refinement process of the red one.

In order to illustrate the influence of the number of clusters, the images resulting from the segmentation step taking into account three and four clusters are shown in Figure 7.

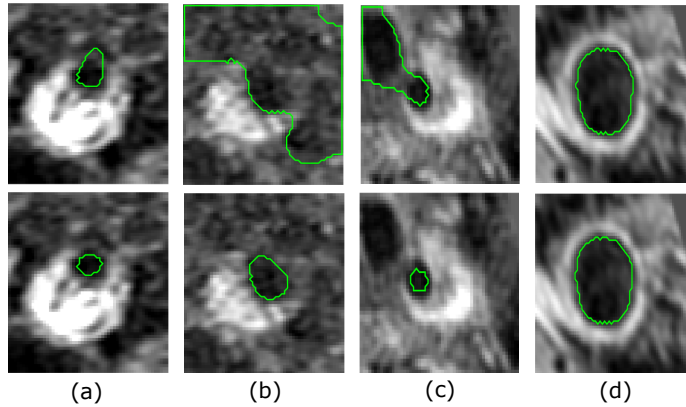


Figure 7: Influence of the number of clusters on the final lumen segmentation: The first row represents the segmentation obtained using three clusters, whereas the second row shows the segmentation obtained using four clusters.

365 As shown in Figure 7a-c, the lumen boundary leaked across the vessel wall when three clusters were used. This is due to the low intensity and the thinness of the vessel wall in the regions where the leakage occurred. The segmentation of the image shown in Figure 7d was not affected by the number of clusters due to the higher grayscale intensity and thickness of the vessel wall.

370 The average values of the Dice similarity, polyline distance, Hausdorff distance and centroid distance of the automatically segmented lumens in comparison to the manual ones are shown in Tables 2 and 3 for each patient, respectively. For each metric, the average standard deviation was calculated using the pooled standard deviation formula.

375 The average measures obtained for the 3D-T1W images were better than those obtained for the PDW images, reaching Dice coefficients ranging from 0.67 ± 0.18 to 0.91 ± 0.04 (Table 2). The maximum Dice coefficient for the PDW images was 0.74 ± 0.16 . This not-so-good result is due to the poor quality of the PDW images when compared to the 3D-T1W images. The polyline and
380 Hausdorff distances were used to assess the difference between the manual and automatic segmentations regarding the contours obtained. For the 3D-T1W images, the polyline distance ranged from 1.06 ± 0.28 to 4.13 ± 5.69 pixels,

Table 2: Average measures obtained for the 3D-T1W images.

	Dice \pm std	PD \pm std (px)	HD \pm std (px)	CD \pm std (px)
Patient 1	0.70 \pm 0.13	2.10 \pm 0.88	5.43 \pm 1.90	2.80 \pm 0.77
Patient 2	0.90 \pm 0.02	1.33 \pm 0.15	2.78 \pm 0.37	0.53 \pm 0.20
Patient 3	0.68 \pm 0.11	1.36 \pm 0.48	2.99 \pm 1.80	1.79 \pm 0.98
Patient 4	0.67 \pm 0.18	2.25 \pm 2.88	6.98 \pm 9.93	3.42 \pm 5.14
Patient 5	0.71 \pm 0.22	1.98 \pm 2.16	4.77 \pm 4.41	1.39 \pm 1.49
Patient 6	0.76 \pm 0.16	2.17 \pm 2.16	8.08 \pm 9.85	3.83 \pm 4.60
Patient 7	0.77 \pm 0.20	1.75 \pm 1.42	4.42 \pm 4.15	1.98 \pm 2.24
Patient 8	0.85 \pm 0.15	1.07 \pm 0.36	2.58 \pm 1.02	1.26 \pm 0.81
Patient 9	0.82 \pm 0.07	1.30 \pm 0.27	3.33 \pm 1.71	1.39 \pm 1.16
Patient 10	0.74 \pm 0.11	1.41 \pm 0.96	4.00 \pm 3.15	1.77 \pm 1.78
Patient 11	0.85 \pm 0.08	1.39 \pm 0.98	3.78 \pm 5.04	1.52 \pm 2.98
Patient 12	0.73 \pm 0.16	4.13 \pm 5.69	9.97 \pm 9.65	5.52 \pm 7.46
Patient 13	0.91 \pm 0.04	1.06 \pm 0.28	3.17 \pm 1.07	1.08 \pm 0.60
Average	0.78 \pm 0.14	1.79 \pm 2.13	4.79 \pm 5.42	2.18 \pm 3.22

*PD=Polyline distance; HD=Hausdorff distance; CD=Centroid distance; px=pixels; std=standard deviation.

Table 3: Average measures obtained for the PDW images.

	Dice \pm std	PD \pm std (px)	HD \pm std (px)	CD \pm std (px)
Patient 1	0.62 \pm 0.12	3.14 \pm 1.14	7.34 \pm 3.52	2.23 \pm 1.64
Patient 2	0.65 \pm 0.25	3.35 \pm 2.48	8.58 \pm 5.90	3.89 \pm 3.05
Patient 3	0.68 \pm 0.10	1.44 \pm 0.59	3.74 \pm 2.42	2.07 \pm 1.21
Patient 4	0.68 \pm 0.21	1.64 \pm 1.30	4.91 \pm 4.11	2.14 \pm 1.42
Patient 5	0.66 \pm 0.14	1.89 \pm 1.34	5.12 \pm 2.87	1.81 \pm 0.93
Patient 6	0.69 \pm 0.15	4.43 \pm 5.75	10.64 \pm 11.55	5.13 \pm 5.72
Patient 7	0.74 \pm 0.16	1.52 \pm 0.93	3.60 \pm 2.07	2.19 \pm 1.49
Patient 8	0.71 \pm 0.26	1.94 \pm 1.63	5.21 \pm 4.83	2.66 \pm 2.86
Patient 9	0.52 \pm 0.23	3.15 \pm 1.99	8.61 \pm 6.08	3.74 \pm 3.03
Patient 10	0.60 \pm 0.25	2.81 \pm 3.22	7.48 \pm 7.78	3.58 \pm 4.24
Patient 11	0.20 \pm 0.26	6.89 \pm 3.76	13.39 \pm 6.27	5.21 \pm 2.41
Patient 12	0.69 \pm 0.24	2.70 \pm 3.19	7.78 \pm 8.96	3.42 \pm 5.00
Patient 13	0.42 \pm 0.23	7.01 \pm 4.98	14.91 \pm 7.62	6.53 \pm 4.37
Average	0.61 \pm 0.21	3.22 \pm 3.05	7.79 \pm 6.47	3.43 \pm 3.35

*PD=Polyline distance; HD=Hausdorff distance; CD=Centroid distance; px=pixels; std=standard deviation.

whereas for the Hausdorff distance the differences ranged from 2.58 ± 1.02 to 9.97 ± 9.65 pixels. On the other hand, for the PDW images, the distances

385 calculated by the polyline distance ranged from 1.44 ± 0.59 to 7.01 ± 4.98
pixels, whereas for the Hausdorff distance the differences ranged from $3.60 \pm$
2.07 to 14.91 ± 7.62 pixels.

As indicated by Table 3, the lower Dice coefficient obtained for patient 11
was due to the fact that the lumen was not well characterized, as shown in
390 Figure 8.

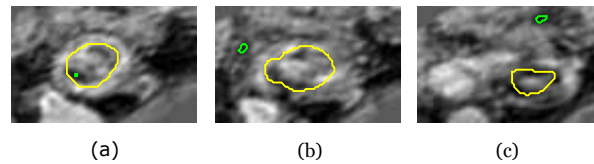


Figure 8: PDW images of patient 11 with the lumen not well characterized (the yellow colour represents the manual delineation, i.e. the correct region of interest).

Figure 8 shows that the K-means algorithm was not able to correctly separate
the whole region into clusters corresponding to the low intensity value because
the region belonging to the lumen under analysis was corrupted by high intensity
values. As mentioned earlier, the high quality of the 3D-T1W images and
395 the good lumen characterization contributed to the good performance of the
proposed method. Some segmentation examples of PDW images with the lumen
properly characterized are shown in Figure 9.

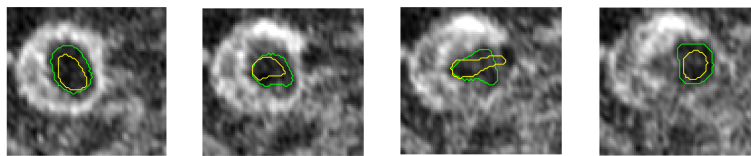


Figure 9: Segmentation of PDW images with the lumen properly characterized (the yellow colour represents the manual delineation, i.e. the correct region of interest).

4. Discussion

The development of automatic methods to correctly identify and segment the
400 lumen in MR images is a challenge considering the low quality of input images,

the presence of stenosis and malformations of this structure. In this work an automatic method to segment the lumen in MR images was presented. Since the lumen is approximately circular in axial MR images, our method automatically evaluated the circularity of the regions segmented by the K-means algorithm. In
405 addition, an active contour algorithm was applied to further refine the boundary of the identified region.

The proposed method has several advantages compared to the other methods found in the literature. The main advantages are that the method is easily implemented and does not need any kind of user interaction. Also, by using
410 a circularity index, the region corresponding to the lumen is identified without the use of complex algorithms. Although the parameters were tuned taking into account the characteristics of the dataset used in this article, most of these characteristics are commonly found in other related datasets, making the chosen parameters also suitable for these datasets without needing to make any significant
415 changes in their values. In terms of the parameters of the pre-processing step, the mask of the median-filter used is a suitable choice to attenuate the noise usually found in medical images without leading to excessive smoothing of the borders of the structures of interest, and is commonly adopted in such studies. The amount of contrast enhancement is determined by the value of the
420 α parameter in Equation 2, which is automatically calculated by using the PDF of the grayscale intensities of the input image. The most important parameters are the ones related to the segmentation step. The number of clusters that are defined has an important role in the proposed method. The grayscale intensity of the lumen in carotid MR images is well-defined and distinguishable from
425 other structures in the images. Hence, the number of clusters proposed here is suitable to be used in other image datasets. Moreover, the number of clusters was defined by taking into account that the thin and low intensity walls of the carotid arteries can cause the lumen boundary to leak. Moreover, since this is a common characteristic found in MR images of carotid arteries, the value of this
430 parameter is appropriate to separate the regions without loss of performance. On using the subtractive clustering algorithm, the r_a and r_b parameters may

affect the number of clusters to be generated [35]. However, since the subtractive clustering is only used to generate the centroids of the expected number of clusters, the values of these parameters can be used in other related image datasets to successfully identify the regions presented according to the same expected number.

Several difficulties that can affect the segmentation accuracy have been addressed in this study. Although the mean roundness measure is an easy and efficient index to identify circular shapes in images, the use of the mean radius also identifies regions not corresponding to a circular pattern, such as the ones that include the border of the input. Hence, additional indexes are employed to penalize the mean roundness index in such cases. Depending on the imaging examination angle, two circular regions corresponding to the internal and external carotid arteries or the jugular vein can appear in the input image, compromising the segmentation result when the circular pattern of such regions is greater than the one of the lumen under study. Therefore, since the lumen is commonly located close to the centre of the input image, the centre index is used to penalize circular regions far from the centre. Consequently, the segmentation results are improved.

The results of the quantitative analysis show the superior quality of the 3D-T1W images which produced better results compared to the PDW images. The centroid distance showed that the location of the segmented lumen corresponds well to the location of the associated manual segmentation, even when there is an under- or over-estimation of the segmented lumen. The maximum average Dice coefficient was 0.91 ± 0.04 for the 181 3D-T1W images, whereas for the 181 PDW images, the maximum average was 0.74 ± 0.16 . On the other hand, the minimum average Dice was 0.67 ± 0.18 and 0.20 ± 0.26 for the same images, respectively. It should be pointed out that the segmentation errors relating to patient 11 contributed to the minimum Dice calculated from the PDW images. The poor quality of the PDW images and the malformation of the lumen contributed to the majority of the segmentation errors found. In addition, the incorrect adjustment of the manual segmentations with respect to the real location of the

lumen could distort the quantitative analysis. Since the manual segmentations were based on a combination of several imaging modalities, a misalignment
465 can exist between such images and the images evaluated here (3D-T1W and PDW MR images). A new set of manual segmentations should be built in order to measure the accuracy of the proposed method against improved manual delineations. Nevertheless, the proposed method was able to identify the correct location of the lumen even in noisy images and in images of only reasonable
470 quality.

The proposed method achieved a total average Dice similarity of 0.78 ± 0.14 for the 181 3D-T1W images and of 0.61 ± 0.21 for the 181 PDW images. Although the validation measures and the type of images used in the majority of related studies are different from the ones presented here, our method is
475 in accordance with the works that have been published. According to Pratt's Figure of Merit (FOM), the method proposed by Yang et al. [24] achieved a similarity of 0.705 between the manually delineated and the segmented lumen contours. Although a complete and simple automatic method to segment the lumen has been proposed by Yang et al. [24], an analysis of the regions in
480 the input images and the application of deformable models may improve the segmentation accuracy. Also, this method presents the following limitations: the applied morphological operations can distort the region corresponding to the lumen, the used gradient based method is not efficient to identify the desired edges on homogeneous regions, and additional algorithms should be employed to
485 refine the boundary found. On the other hand, the method proposed by Adame et al. [22] achieved a correlation coefficient r of 0.94 between the manually delineated and the segmented lumen contours. However, all regions of the input image are processed to find the correct lumen, instead of evaluating only the regions limited by the wall boundary. In addition, the method proposed by Gao
490 et al. [25] achieved a correlation coefficient r equal to 0.99 in the segmentation of the lumen in IVUS images. However, the lumen segmentation is performed after the identification of the region corresponding to the media-adventitia layer.

Manual editing could be considered to improve the results of the proposed

method by manually adjusting the detected contour towards the real boundary
495 of the lumen, leading to lower segmentation errors and, consequently, higher
Dice coefficients. However, this would lead to a more time-consuming and sub-
jective solution.

In spite of the potential offered by the proposed method, some limitations
exist. Since the images showed regions of interest (ROI) acquired from the
500 MRI exam, no additional pre-processing or delineation to limit the ROI was
performed in the input images. However, the cropping of medical images rep-
resents an important step to generate the regions surrounding the structures
of interest. Since the MRI scan of carotid arteries is performed using a large
field of view, covering the whole region of the neck, the cropping of the images
505 becomes necessary to remove undesirable structures. Centerline tracking algo-
rithms [36, 37] represent an alternative to find the centre of the artery in each
slice and crop the image in order to obtain the region surrounding that artery.
The success of the segmentation depends on correctly setting up the parameters
of the proposed method, mainly the percentage of disregarded regions, which
510 depends on the resolution of the input image. Since small regions corresponding
to noisy artifacts can also appear as circular regions in some cases, the proposed
method can fail to identify the correct lumen in these cases. The higher the im-
age resolution is, the higher the percentage of disregarded regions should be.
However, special attention must be taken when the lumen appears as a small
515 region in the input image since it can also be discarded when a high percentage
of disregarded regions is adopted. Although morphological operations could be
effective to remove noisy regions from the input image, the choice of the shape
and size of the structuring element is relevant to remove any noise efficiently and
avoid the distortion of the region corresponding to the lumen. A more efficient
520 approach will be considered in the future in order to correctly identify regions
corresponding to noise without having to use ‘disregarding percentages’.

5. Conclusions

The development of a fully automatic segmentation method of the lumen and vessel wall is an-ongoing and intensive focus of research. In this article
525 a novel method was presented for the automatic lumen segmentation in MR images of the carotid artery without user interaction. The proposed method proved to be promising to identify the correct location of the lumen.

The low quality of the input images and the malformation of the lumen, as well as the misalignment and lack of manual interventions, contributed to the
530 majority of the segmentation errors found. Nevertheless, the results showed that a good overlap and low point distances between the automatically segmented lumen and the associated manual results can be achieved by the proposed method even in the presence of noise.

Future studies will be conducted to reduce the number of parameters used in
535 the proposed method and to tune automatically their values based on features of the input image. In addition, the segmentation of the vessel wall is going to be addressed in the next step of our research.

Acknowledgements

This work was partially funded by Coordenação de Aperfeiçoamento de Pes-
540 soal de Nível Superior (CAPES), funding agency in Brazil, under the PhD Grant with reference number 0543/13-6.

The authors thank the funding of Project NORTE-01-0145-FEDER-000022 - SciTech - Science and Technology for Competitive and Sustainable Industries, co-financed by “Programa Operacional Regional do Norte” (NORTE2020),
545 through “Fundo Europeu de Desenvolvimento Regional” (FEDER).

References

- [1] L. C. Sousa, C. F. Castro, C. C. António, A. Santos, R. Santos, P. Castro, E. Azevedo, J. M. R. Tavares, Haemodynamic conditions of patient-

- specific carotid bifurcation based on ultrasound imaging, *Computer Meth-*
ods in Biomechanics and Biomedical Engineering: Imaging & Visualization
2 (2014) 157–166.
- [2] L. C. Sousa, C. F. Castro, C. C. António, A. M. F. Santos, R. M. Santos,
P. M. A. C. Castro, E. Azevedo, J. M. R. S. Tavares, Toward hemodynamic
diagnosis of carotid artery stenosis based on ultrasound image data and
computational modeling, *Medical & Biological Engineering & Computing*
52 (2014) 971–983.
- [3] K. L. Furie, S. M. Smimakis, W. J. Koroshetz, J. P. Kistler, Stroke due to
large artery atherosclerosis, in: K. L. Furie, P. J. Kelly (Eds.), *Handbook of
Stroke Prevention in Clinical Practice, Current Clinical Neurology*, Humana
Press, 2004, pp. 151–165.
- [4] J. P. Schadé, *The Complete Encyclopedia of Medicine & Health*, Foreign
Media Books, 2006.
- [5] D. O. Wiebers, V. L. Feigin, R. Brown, *Handbook of Stroke, Board Review
Series*, 2 ed., Lippincott Williams & Wilkins, Philadelphia, PA, 2006.
- [6] D. S. Jodas, A. S. Pereira, J. M. R. Tavares, A review of computa-
tional methods applied for identification and quantification of atheroscle-
rotic plaques in images, *Expert Systems with Applications* 46 (2016) 1 –
14.
- [7] W. Kerwin, D. Xu, F. Liu, T. Saam, H. Underhill, N. Takaya, B. Chu,
T. Hatsukami, C. Yuan, Magnetic resonance imaging of carotid atheroscle-
rosis: plaque analysis., *Topics in Magnetic Resonance Imaging : TMRI* 18
(2007) 371–378.
- [8] L. Saba, H. Gao, E. Raz, S. V. Sree, L. Mannelli, N. Tallapally, F. Molinari,
P. P. Bassareo, U. R. Acharya, H. Poppert, J. S. Suri, Semiautomated anal-
ysis of carotid artery wall thickness in MRI, *Journal of Magnetic Resonance
Imaging* 39 (2014) 1457–1467.

- [9] A. van Engelen, W. J. Niessen, S. Klein, H. C. Groen, H. J. M. Verhagen, J. J. Wentzel, A. van der Lugt, M. de Bruijne, Atherosclerotic plaque component segmentation in combined carotid MRI and CTA data incorporating class label uncertainty, *PLoS ONE* 9 (2014) 1–14.
580
- [10] D. Vukadinovic, T. Van Walsum, S. Rozie, T. de Weert, R. Manniesing, A. van der Lugt, W. Niessen, Carotid artery segmentation and plaque quantification in CTA, in: *IEEE International Symposium on Biomedical Imaging: From Nano to Macro, 2009*, pp. 835–838. doi:10.1109/ISBI.2009.5193182.
585
- [11] D. Vukadinovic, T. Van Walsum, R. Manniesing, S. Rozie, R. Hameeteman, T. de Weert, A. van der Lugt, W. Niessen, Segmentation of the outer vessel wall of the common carotid artery in CTA, *IEEE Transactions on Medical Imaging* 29 (2010) 65–76.
- [12] R. van 't Klooster, A. J. Patterson, V. E. Young, J. H. Gillard, J. H. C. Reiber, R. J. van der Geest, An Objective Method to Optimize the MR Sequence Set for Plaque Classification in Carotid Vessel Wall Images Using Automated Image Segmentation, *PLoS ONE* 8 (2013) 1–7.
590
- [13] A. van Engelen, W. J. Niessen, S. Klein, H. C. Groen, H. J. Verhagen, J. J. Wentzel, A. van der Lugt, M. de Bruijne, Supervised in-vivo plaque characterization incorporating class label uncertainty, in: *9th IEEE International Symposium on Biomedical Imaging (ISBI), IEEE, 2012*, pp. 246–249.
595
- [14] B. Chiu, V. Shamdasani, R. Entrekin, C. Yuan, W. S. Kerwin, Characterization of carotid plaques on 3-dimensional ultrasound imaging by registration with multicontrast magnetic resonance imaging, *Journal of Ultrasound in Medicine: Official Journal of the American Institute of Ultrasound in Medicine* 31 (2012) 1567–1580.
600
- [15] A. Fenster, A. Landry, D. B. Downey, R. A. Hegele, J. D. Spence, 3D ultrasound imaging of the carotid arteries, *Current Drug Targets - Cardiovascular & Hematological Disorders* 4 (2004) 161–175.
605

- [16] A. Fenster, G. Parraga, J. Bax, Three-dimensional ultrasound scanning, *Interface Focus* 1 (2011) 503–519.
- [17] M. M. Hossain, K. AlMuhanna, L. Zhao, B. K. Lal, S. Sikdar, Three dimensional level set based semiautomatic segmentation of atherosclerotic carotid artery wall volume using 3D ultrasound imaging, *Medical Physics* 9034 (2014) 90344B–1–90344B–8.
- [18] E. Ukwatta, J. Awad, A. Ward, J. Samarabandu, A. Krasinski, G. Parraga, A. Fenster, Segmentation of the lumen and media-adventitia boundaries of the common carotid artery from 3D ultrasound images, in: *Progress in Biomedical Optics and Imaging - Proceedings of SPIE*, volume 7963, 2011, pp. 79630G–1–79630G–8. doi:10.1117/12.877722.
- [19] V. Caselles, R. Kimmel, G. Sapiro, Geodesic active contours, in: *Proceedings of IEEE International Conference on Computer Vision*, IEEE Comput. Soc. Press, 1995, pp. 694–699. doi:10.1109/ICCV.1995.466871.
- [20] T. F. Chan, L. A. Vese, Active contours without edges, *IEEE Transactions on Image Processing* 10 (2001) 266–277.
- [21] Z. Ma, J. M. R. Tavares, R. N. Jorge, T. Mascarenhas, A review of algorithms for medical image segmentation and their applications to the female pelvic cavity, *Computer Methods in Biomechanics and Biomedical Engineering* 13 (2010) 235–246.
- [22] I. M. Adame, R. J. van der Geest, B. A. Wasserman, M. Mohamed, J. H. Reiber, B. P. Lelieveldt, Automatic plaque characterization and vessel wall segmentation in magnetic resonance images of atherosclerotic carotid arteries, in: *Medical Imaging 2004, International Society for Optics and Photonics*, 2004, pp. 265–273.
- [23] I. M. Adame, R. J. van der Geest, B. A. Wasserman, M. A. Mohamed, J. H. Reiber, B. P. Lelieveldt, Automatic segmentation and plaque characteri-

- zation in atherosclerotic carotid artery MR images, *Magnetic Resonance Materials in Physics, Biology and Medicine* 16 (2004) 227–234.
- 635 [24] X. Yang, M. Ding, L. Lou, M. Yuchi, W. Qiu, Y. Sun, Common carotid artery lumen segmentation in B-mode ultrasound transverse view images, *International Journal of Image, Graphics and Signal Processing (IJIGSP)* 3 (2011) 15–21.
- [25] Z. Gao, W. K. Hau, M. Lu, W. Huang, H. Zhang, W. Wu, X. Liu, Y.-T. Zhang, Automated Framework for Detecting Lumen and MediaAdventitia Borders in Intravascular Ultrasound Images, *Ultrasound in Medicine & Biology* 41 (2015) 2001–2021.
- 640 [26] A. M. F. Santos, J. M. R. S. Tavares, L. Sousa, R. Santos, P. Castro, E. Azevedo, Automatic segmentation of the lumen of the carotid artery in ultrasound B-mode images, *Proc. SPIE* 8670 (2013) 86703I–86703I–16.
- 645 [27] A. M. F. Santos, R. M. dos Santos, P. M. A. Castro, E. Azevedo, L. Sousa, J. M. R. S. Tavares, A novel automatic algorithm for the segmentation of the lumen of the carotid artery in ultrasound B-mode images, *Expert Systems with Applications* 40 (2013) 6570–6579.
- [28] S.-C. Huang, F.-C. Cheng, Y.-S. Chiu, Efficient Contrast Enhancement Using Adaptive Gamma Correction with Weighting Distribution, *IEEE Transactions on Image Processing* 22 (2013) 1032–1041.
- 650 [29] K. Bataineh, M. Najj, M. Saqer, A comparison study between various fuzzy clustering algorithms, *Editorial Board* 5 (2011) 335–343.
- [30] N. Dhanachandra, K. Manglem, Y. J. Chanu, Image Segmentation Using K -means Clustering Algorithm and Subtractive Clustering Algorithm, *Procedia Computer Science* 54 (2015) 764–771.
- 655 [31] Y. Kehong, Z. Jiying, F. Shu, D. Chaijie, B. Shanglian, C. Qiansheng, Roundness curve for classification of cell phase on microscopic image, in:

- 660 International Conference on Technology and Applications in Biomedicine
(ITAB), 2008, pp. 70–73.
- [32] N. Ritter, J. Cooper, New Resolution Independent Measures of Circularity,
Journal of Mathematical Imaging and Vision 35 (2009) 117–127.
- [33] A. M. Herrera-Navarro, H. Jiménez Hernández, H. Peregrina-Barreto,
665 F. Manríquez- Guerrero, I. R. Terol-Villalobos, A New Measure of Cir-
cularity Based on Distribution of the Radius, Computación y Sistemas 17
(2013) 515–526.
- [34] S. Jain, V. Jagtap, N. Pise, Computer Aided Melanoma Skin Cancer De-
tection Using Image Processing, Procedia Computer Science 48 (2015)
670 735–740.
- [35] S. L. Chiu, Fuzzy model identification based on cluster estimation, Journal
of Intelligent & fuzzy systems 2 (1994) 267–278.
- [36] M. M. G. Macedo, C. Mekkaoui, M. P. Jackowski, Vessel Centerline
Tracking in CTA and MRA Images Using Hough Transform, Springer
675 Berlin Heidelberg, Berlin, Heidelberg, 2010, pp. 295–302. doi:10.1007/
978-3-642-16687-7_41.
- [37] H. Tang, T. van Walsum, R. S. van Onkelen, S. Klein, R. Hameeteman,
M. Schaap, Q. J. A. van den Bouwhuisen, J. C. M. Witteman, A. van der
Lugt, L. J. van Vliet, W. J. Niessen, Multispectral MRI centerline tracking
680 in carotid arteries, in: SPIE Medical Imaging, volume 7962, 2011, pp.
79621N–1–79621N–7. doi:10.1117/12.877817.